

1 Carbon coated TiO₂ nanoparticles prepared by pulsed laser 2 ablation in liquid, gaseous and supercritical CO₂

3 Amandeep Singh*¹, Turkka Salminen², Mari Honkanen², Juha-Pekka Nikkanen¹, Tommi Vuorinen³,
4 Risto Kari¹, Jorma Vihinen⁴, Erkki Levänen¹

5 ¹Materials Science and Environmental Engineering Unit, Faculty of Engineering and Natural Sciences, P.O. Box
6 527 FI-33014 Tampere University, Tampere, Finland

7 ²Tampere Microscopy Center, P.O. Box 692, FI-33014 Tampere University, Tampere, Finland

8 ³VTT Technical Research Centre of Finland Ltd, PO Box 1300, FI-33101 Tampere, Finland

9 ⁴Mechanical Engineering Unit, Faculty of Engineering and Natural Sciences, P.O. Box 527 FI-33014, Tampere
10 University, Tampere, Finland

11 *Corresponding author: Amandeep Singh – amandeep.singh@tuni.fi

12

13 Abstract

14 We report on the synthesis of TiO₂ nanoparticles using nanosecond pulse laser ablation of titanium in
15 liquid, gaseous and supercritical CO₂. The produced particles were observed to be mainly anatase--
16 TiO₂ with some rutile-TiO₂. In addition, the particles were covered by a carbon layer. Raman and X-ray
17 diffraction data suggested that the rutile content increases with CO₂ pressure. The nanoparticle size
18 decreased and size distribution became narrower with the increase in CO₂ pressure and temperature,
19 however the variation trend was different for CO₂ pressure compared to temperature. Pulsed laser
20 ablation in pressurized CO₂ is demonstrated as a single step method for making anatase-TiO₂/carbon
21 nanoparticles throughout the pressure and temperature ranges 5–40 MPa and 30–50 °C, respectively.

22 Keywords: pulsed laser ablation, core-shell particles, supercritical fluids, nanoparticle size control

1 Introduction

2 Titanium dioxide is among the most studied nanomaterials as it an important photocatalytically active
3 material with applications such as in water purification [1], lithium ion batteries [2], and solar cells [3].
4 Combining TiO₂ with carbon nanostructures such as graphene to form graphene/TiO₂ heterostructures
5 has been reported as a new optical and electronic device platform with dual functionality of field effect
6 and photosensitivity in bottom gated field effect transistors [4]. In another study, the presence of
7 core-shell TiO₂-carbon structures as a support material was reported to enhance the catalytic activity
8 of a Pt catalyst and improve its stability in direct methanol fuel cells compared to traditionally used Pt
9 catalyst with carbon black support [5]. Core shell nanoparticles of various compositions have extensive
10 applications and have been well highlighted in the recent reviews reporting their use in catalysis and
11 electrocatalysis [6], energy storage and conversion (such as in lithium ion batteries, supercapacitors,
12 and quantum dot solar cells) [7], and medical biotechnology (such as in molecular bioimaging, drug
13 delivery, and cancer treatment) [8]. Techniques for preparing core-shell nanoparticles include
14 chemical vapour deposition [9], wet-chemistry based methods such as sol-gel synthesis [10], and
15 polymerization [11], physical methods such as flame synthesis [12], plasma-based synthesis [13,14]
16 and spray pyrolysis [15]. Pulsed laser ablation in liquids (PLAL) for core-shell nanoparticle generation
17 [16] is another physical method that, similar to the other physical methods, is an in-situ synthesis
18 process, requires little sample preparation, few synthesis steps and unlike in wet-chemistry methods,
19 does not require environmentally hazardous solvents. Due to high yield relative to solid educt mass
20 and no waste of reagents, it may further save waste management and disposal costs compared to
21 chemical methods [17].

22 PLAL is often called a green technique as it can be used to synthesize nanoparticles without the need
23 of toxic chemicals [17]. The synthesis of well-dispersed unagglomerated nanoparticles of titanium
24 oxides has been demonstrated in supercritical carbon dioxide (scCO₂) [18]. In the supercritical state,
25 CO₂ may penetrate and leave nanostructures unharmed due to absence of surface tension. The
26 surrounding fluid in pulsed laser ablation (PLA) plays an important role on the phase, structure and

1 morphology of nanoparticles. In the first study on PLA of gold in scCO₂, Saitow et al. reported that
2 nanoparticles consisted of two size distributions: nanoparticles with average diameters 30 nm and
3 around 500 nm [19]. Production of nanoparticles from various materials has been reported using PLA
4 in scCO₂. The target materials include silicon [20], gold [19], silver [21], copper [22], pyrolytic graphite
5 [23] and titanium [18]. In addition to the laser parameters and the ablated material, the CO₂
6 temperature and pressure is important as it changes the properties of scCO₂ to be either liquid-like or
7 gas-like which may further affect the nanoparticle size, morphology and phase. In a previous study,
8 the effect of scCO₂ pressure, density and temperature on a gold target has been reported [24].
9 However, there are no studies on generation of core-shell nanoparticles by PLA when CO₂ is in the
10 supercritical regime, to the best of our knowledge. Previously, PLA in pressurized CO₂ has been
11 demonstrated to form metal-core carbon-shell nanoparticles of Ni-carbon in gaseous CO₂ [25] and Au-
12 carbon in liquid and gaseous CO₂ [26].

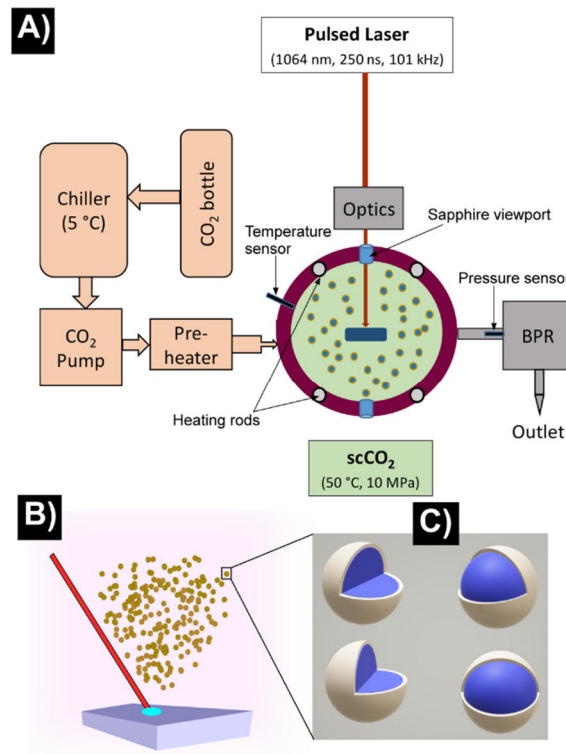
13 This study demonstrates single-step synthesis of TiO₂-carbon core-shell nanoparticles from titanium
14 by PLA in pressurized CO₂ in liquid, gaseous and supercritical state. This demonstrates the potential of
15 PLA in scCO₂ for synthesis of core-shell particles. We report on the effect of CO₂ pressure and
16 temperature on the size, size distribution and phase of core-shell nanoparticles synthesized in liquid,
17 gaseous and scCO₂. The effect of different test condition i.e. supercritical state CO₂ against liquid and
18 gaseous CO₂ is also reported. PLA in pressurized CO₂ was carried out using a 250 ns pulse fiber laser
19 with wavelength of 1062nm and repetition rate of 101 kHz to synthesize nanoparticles. (S)TEM
20 (Scanning transmission electron microscopy), XPS (X-ray photoelectron spectroscopy), Raman, XRD (X-
21 ray diffraction), and ultraviolet-visible (UV-Vis) spectroscopy techniques were used to study the
22 synthesized nanoparticles and evaluate the effect of CO₂ pressures 5–40 MPa and temperatures 30–
23 50 °C on the nanoparticle size, size distribution and phase.

24 Experimental

25 Nanosecond laser ablation in liquid, gaseous and supercritical CO₂:

1 Pulsed laser ablation in CO₂ was carried out using a 250 ns pulse fiber laser with wavelength of 1062
2 nm, and repetition rate of 101 kHz. The laser beam was focused using an 80 mm telecentric f-Theta
3 lens to a spot diameter of 35 μm on the titanium target and scanned on an area of 64 mm². The beam
4 energy was 690 μJ per pulse for 101 kHz repetition rate. The experimental set-up consisted of a
5 titanium target (99.99% pure, Goodfellow Cambridge Ltd) fitted inside the autoclave (made of
6 stainless steel 316 with pressure and temperature limits of 62 MPa and 150 °C, respectively) in such a
7 way that it could be scanned with the laser through the sapphire optical viewport as shown in the
8 schematic (figure 1(a)). Figure 1(b) shows the schematic inside the autoclave where laser irradiates
9 the target and nanoparticles are synthesized. Figure 1(c) shows a schematic of these nanoparticles
10 that consisted of mostly core-shell nanoparticles. The ablation experiments were conducted at five
11 different CO₂ pressures: 5, 10, 15, 20 and 40 MPa. CO₂ (> 99.8 % pure) was pumped into the autoclave
12 with a high-pressure piston pump. CO₂ was cooled to 5 °C in the chiller before being pumped. Between
13 the pump and the autoclave, CO₂ passed through a heat exchanger where it was warmed and
14 converted to scCO₂. The heating rods, installed in the walls of the autoclave, were used to heat it to
15 30, 40, and 50 °C for the corresponding experiments. After the temperature and pressure stabilized at
16 the desired value, the target was ablated with the laser for 30 minutes using a scanning speed of 2
17 m/s to cover a 7×7 mm pattern. To collect the nanoparticle powder, the autoclave was depressurized
18 with an automatic backpressure regulator at a rate of 5 seconds/MPa. The pressure sensor with an
19 accuracy of 0.05 MPa was located just before the inlet valve of backpressure regulator while the
20 temperature sensor with accuracy of 1.1 °C was located inside the chamber. This study comprised of
21 seven PLA tests in pressurized CO₂, five in scCO₂, one in liquid CO₂ and one in gaseous CO₂. To study
22 the effect of CO₂ pressure and temperature, the tests may be divided in two parts: (1) CO₂ temperature
23 fixed at 50 °C while five different pressures 5, 10, 15, 20, and 40 MPa were tested, and (2) CO₂ pressure
24 fixed at 10 MPa while different temperatures 30, 40 and 50 °C were tested. The pressure and
25 temperature values of these tests are marked in figure 2a. In figure 2(b), the symbols represent the
26 densities for the selected CO₂ parameters in this study while the standard curves taken from the

1 National Institute of Standards and Technology, U.S. Department of Commerce [27] show the variation
2 of CO₂ density with pressure for three temperatures 30, 40, and 50 °C.



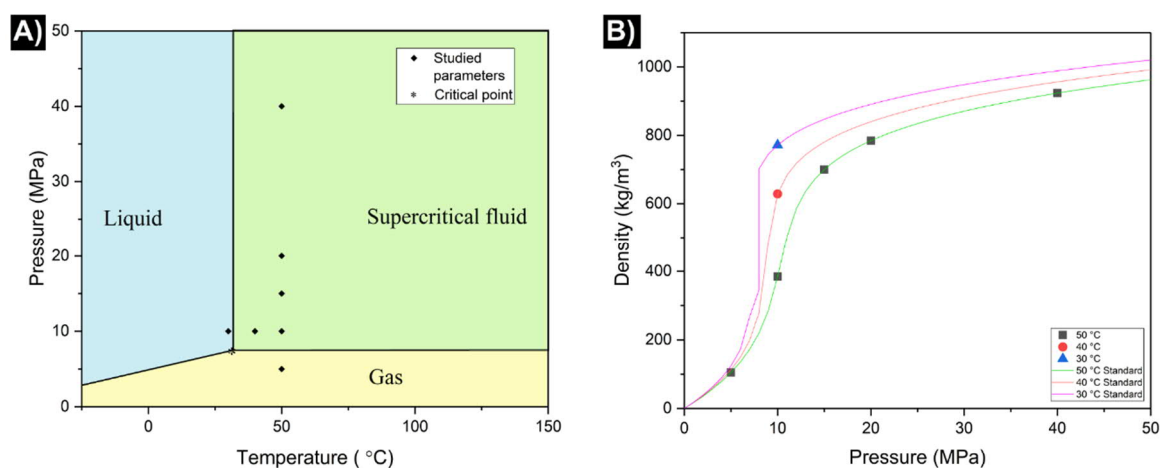
3
4 Figure 1 shows (a) schematic of the experimental setup, (b) schematic of ablation of titanium to produce nanoparticles, (c)
5 synthesized nanoparticles consist of core-shell type nanoparticles.

6 Characterization methods:

7 The nanoparticle powders were characterized by using a Jeol-JEM F200 (S)TEM with a Jeol Dual
8 electron energy dispersive spectrometer (EDS), Renishaw InVia Qontor Raman microscope, Panalytical
9 Empyrean Multipurpose Diffractometer for XRD, PHI Quantum 2000 for XPS and by Shimadzu
10 spectrophotometer for determination of band-gap energy.

11 For (S)TEM, the samples were prepared by touching the TEM copper grid containing holey carbon film
12 with the nanoparticle powder. From the TEM images, diameters of 400 nanoparticles were measured
13 using Image J software (Version 1.50i) and to estimate the size distributions and average particle size
14 for each sample. STEM-EDS was used in line analysis and spot analysis mode to analyse the variation
15 in the elemental composition of the nanoparticles and the layer on them. Phase analysis of the

1 nanoparticle powders was analysed with the Renishaw InVia Qontor Raman microscope using a 532
 2 nm laser. The laser power was 0.175 μ W. The XRD patterns of the nanoparticle powders were obtained
 3 using the Panalytical Empyrean Multipurpose Diffractometer with a CuK α X-ray source at wavelength
 4 of 0.1541 nm. The scattered intensities were measured using a solid-state pixel detector, PIXcel3D
 5 attached to the diffractometer. The X-ray generator operating values were 45 kV and 40 mA. The data
 6 was collected in the range of $2\theta = 10.00\text{--}80.00^\circ$ and for a step size of $2\theta = 0.02^\circ$. Panalytical HighScore
 7 Plus software (version 3.0.5) was used for the identification of phases in the XRD pattern based on the
 8 database PDF-4 + of the International Centre for Diffraction data (version 4.1065). The XPS analysis
 9 was performed with PHI Quantum 2000 spectrometer with an Al 1486.6 eV mono X-ray source at 24.3
 10 W. The XPS sample was prepared carefully spreading the nanoparticle powder on top of a double-
 11 sided tape that was attached to a metal plate. The measurement was done with a stationary beam
 12 with a beam diameter of 100 μ m. The optical properties of the material were studied using a
 13 spectrophotometer (Shimadzu UV 3600) in reflectance mode. The absorbance spectra were measured
 14 for the wavelength range 300–900 nm. The plotted Tauc-plots were used to estimate the band-gap
 15 energy of the material.



16
 17 Figure 2 (a) Experimental parameters used in this study are plotted on CO₂ phase diagram, (b) CO₂ densities corresponding
 18 to the experimental parameters used are plotted against the standard CO₂ curves at 30, 40 and 50 °C.

1 Results and discussion

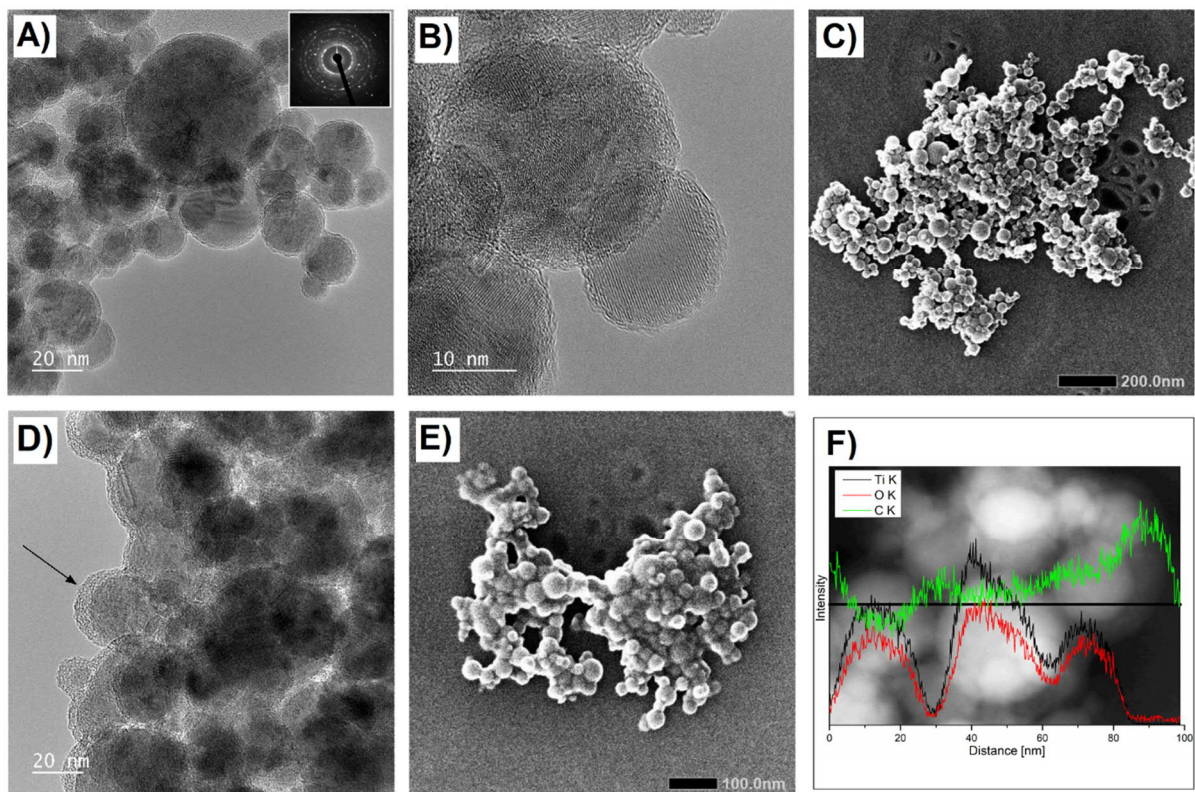
2 The visual appearance of the nanoparticles was bluish-white when the autoclave was opened and did
3 not change during several months of storage. The nanoparticles were in the form of dry and loose
4 powder. The results and discussion is divided into two sections. First section deals with the analysis of
5 nanoparticles synthesized at 10 MPa, 50 °C, while the second section deals with the effect of CO₂
6 pressure and temperature on the nanoparticle size, size distribution and phase.

7 Section 1: Morphology, composition, phase analysis and band-gap measurement of 8 nanoparticles synthesized at 10 MPa, 50 °C.

9 Morphology and composition of nanoparticles

10 The (S)TEM images (Figure 3 (a–f)) showed presence of round nanoparticles that formed clusters or
11 networks. Such nano-networks formed by ablation in scCO₂ have been previously reported [19].
12 Electron diffraction patterns indicated crystallinity of these nanoparticles (figure 3(a) inset). Based on
13 the lattice fringes, some particles were single crystals while others were polycrystalline. On the basis
14 of (S)TEM images, the nanoparticles can be classified into two types: (i) core-shell nanoparticles
15 (Figure 3(a, b, c)), and (ii) nanoparticles surrounded by thick layer (Figure 3(d, e)). In case of core-shell
16 nanoparticles, the shell surface was smooth and the thickness of the shell varied from particle to
17 particle. Jung et al. [28] also reported varying shell thickness and observed increase in the carbon shell
18 thickness with the increase in the core-shell nanoparticles size.. For clusters with thicker carbon layer,
19 the nanoparticles did not appear to be typical core-shell structures as the layer surrounded several
20 nanoparticles (figure 3(d)). This is further elucidated from the backscattered electron (BSE) image
21 (topographical mode) in figure 3(e) where particles seemed to be buried under thick layer. In such
22 cases, the particles seemed to form clusters first after which carbon layer may grow on top of them.
23 The nanoparticles, in figure 3(d), with a thick surface layer were rarer than the core-shell structures
24 on the TEM grid, making the core-shell nanoparticles to be the dominant species. This has been
25 previously reported in pulsed laser ablation of iron-gold where over 90% of nanoparticles consisted of

1 a core-shell morphology [29]. In our study, samples from each test condition consisted of two
2 populations of nanoparticles covered with either thin or thick carbon layer. We did not observe a
3 significant change in the shell thickness in either population nor any change in the relative amount of
4 the two populations as the process parameters were varied. STEM-EDS line analysis (figure 3f) and
5 spot analysis indicated that nanoparticle core consisted of mostly titanium and oxygen, while the
6 shell/surface layer consisted of carbon. A drop in the titanium, oxygen peak intensities and a surge in
7 the carbon peak intensity was observed between 80-100 nm (figure 3f). A dramatic change in carbon
8 peak intensity at the center of particles is not observed as it is a cluster of nanoparticles. They can be
9 considered as 3D spheres with surface shell and the electron beam interacts with them orthogonally.
10 This implies that there will always be some carbon intensity in the STEM-EDS spectra, higher than for
11 titanium and oxygen. In addition, the TEM grid also has a holey carbon film, as mentioned earlier in
12 the experimental section.



13

14 Figure 3 Nanoparticles with thin carbon layer: (a) TEM images of core-shell type nanoparticles and electron diffraction
15 pattern (inset) indicating crystalline particles, (b) high-resolution TEM image of the single crystal particle (marked by an

1 arrow) with lattice fringes corresponding to anatase (101), (c) STEM BSE image (topographical mode) of core-shell
2 nanoparticles. Nanoparticles with thick carbon layer: (d) TEM image of nanoparticles covered with a thick carbon layer,
3 marked by an arrow, (e) STEM BSE image (topographical mode) of nanoparticles with a thick carbon layer, and (f) STEM-
4 EDS line analysis of nanoparticles showing intensity variation of Ti, O and C.

5 Raman and XRD analysis of nanoparticles

6 Raman measurements of the synthesized nanoparticles indicated presence of mostly anatase-TiO₂
7 with small amounts of rutile-TiO₂ (figure 4(a)). The strongest peaks in Raman spectra at around 144,
8 400, 520, and 636 cm⁻¹ corresponded to anatase-TiO₂. The peaks corresponding to rutile at around
9 447 and 610 cm⁻¹ can be observed as small features and shoulders in the anatase spectrum. XRD
10 supports Raman results indicating presence of mostly anatase-TiO₂. Sharp distinct peaks of anatase
11 were observed at 25.3, 48.1, 54.1 and 55.2 2θ degrees (figure 4(b)). The other remaining peaks of
12 anatase observed are marked in the figure. Other peaks in the XRD spectrum could be explained by
13 rutile-TiO₂ at 27.4, titanium oxide carbide Ti₍₁₎O_(0.5)C_(0.5) at 42.1 and 36.2 2θ degrees, and brookite-TiO₂
14 at 30.8 2θ degrees. No graphitic-carbon peaks at 26.1 and 42.3 2θ degrees could be distinctly
15 observed; however, amorphous nature of carbon may have caused the broad pedestal starting from
16 under the anatase peak at 25.3 until the peak for brookite at 30.8. As reported by Marzum et al. in a
17 study of core-shell nanoparticles synthesized by PLA in liquids, it is difficult to observe amorphous
18 carbon on nanoparticles by XRD technique as it is more suitable for crystalline materials [30]. Thus,
19 Raman and XRD spectra suggest anatase-TiO₂ as the main phase of nanoparticles with small amount
20 of rutile-TiO₂, and in addition XRD suggests presence of brookite-TiO₂ and carbon containing phase
21 Ti₍₁₎O_(0.5)C_(0.5). Further, the peaks for TiC were missing from both Raman and XRD spectra, suggesting
22 carbon may not be chemically bonded to titanium. Additionally, for wide spectrum measurement
23 (figure 4(a) inset), Raman spectra showed a broad feature centered at about 1100 cm⁻¹ and near 1450
24 cm⁻¹. As the D and G bands are not observed, this suggests that the carbon on top of the samples is
25 possibly due to hydrocarbons rather than pure carbon. The peak at 1100 cm⁻¹ can be attributed to C-
26 C bond stretching whereas the feature at 1450 cm⁻¹ can be attributed to CH₂ twists and bends.

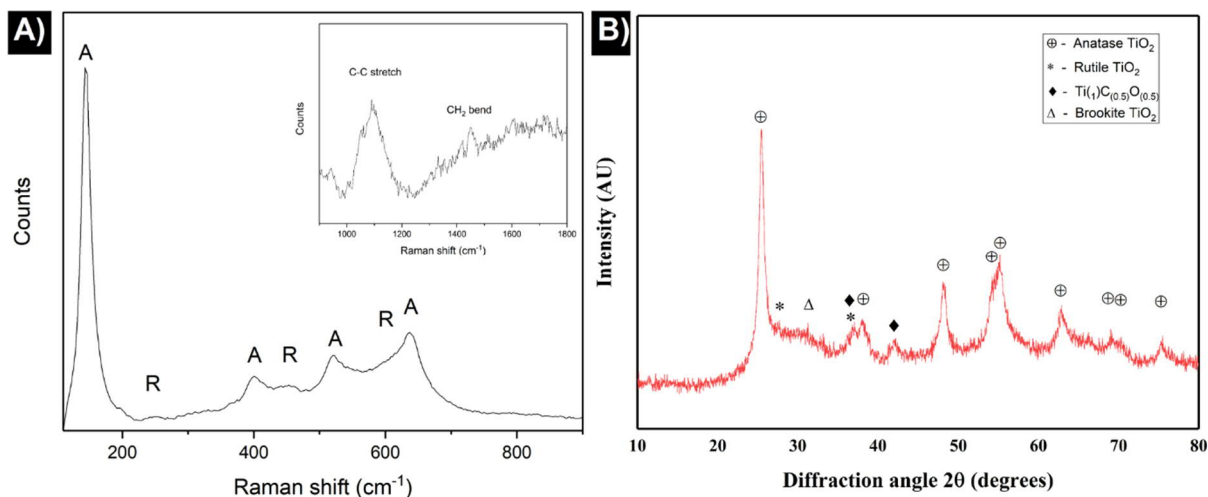
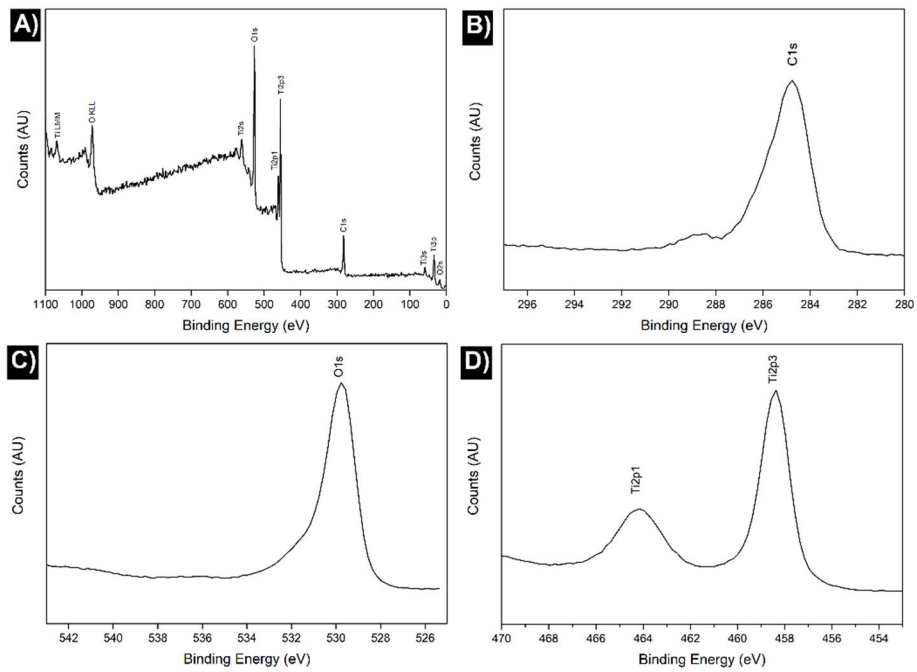


Figure 4 (a) Raman spectra and (b) XRD spectra of the nanoparticles synthesized at 10 MPa, 50 °C.

XPS analysis of nanoparticles

In the XPS spectra of the sample (figure 5(a)), peaks for Ti2p, O1s and C1s were observed. In figure 5(b), C1s peak between 284 eV and 286 eV indicated presence of carbon in sp² hybridization, C=C. The broadening of this peak around 286-287 may indicate presence of also sp³ carbon. Peak between 288 eV and 290 eV was likely from O-C=O. Carbon-titanium bonds would cause peaks at 281.5 eV, 454.7 eV, and 460.9 eV, which were not observed. The peak in XPS spectra figure 5(c) corresponds to the O1s peak at 530 nm. The shoulder to this peak at 532 nm likely comes from organic C=O (531.5-532 nm) indicating possible presence of organic carbonyl, ketones or it may likely be from the H-O-C bond. Metal carbonate, such as TiCO₃ (531.5-532 nm) may possibly add to this feature at 532 nm. Ti 2p_{1/2} and Ti 2p_{3/2} peaks at 464.3 eV and 458.5 eV respectively observed in the XPS spectra (figure 5d) indicated presence of titanium in +4 oxidation state Ti(IV) and the band energies corresponded to anatase-TiO₂ and rutile-TiO₂. XPS results were in accordance with Raman and XRD results to indicate presence of anatase and rutile and further suggested presence of carbon on the nanoparticles, which was not observed to be bonded to titanium.

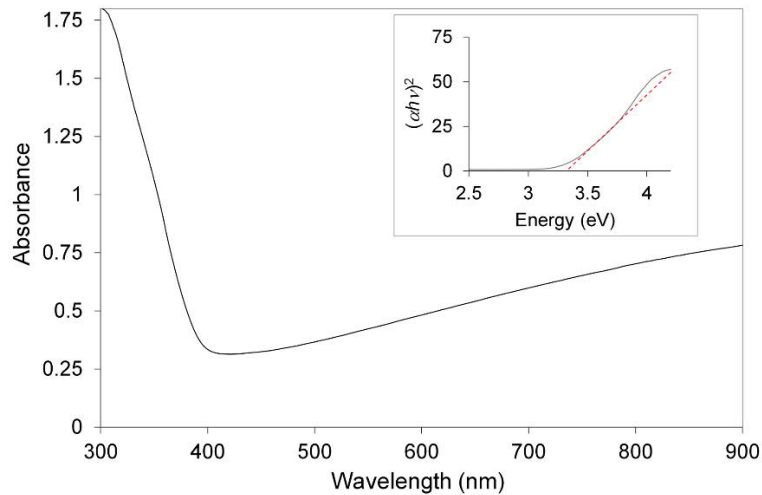


1

2 Figure 5 (a) XPS spectra of nanoparticles synthesized at 10 MPa, 50 °C, (b) carbon C1s peak, (c) O1s peak, (d) Ti2p doublet
 3 peaks in high resolution XPS spectra

4 Band-gap measurement

5 The band gap of the nanoparticles was calculated to be 3.32 eV from the reflectance spectra using the
 6 Tauc plot (figure 6). The bulk value for anatase is reported as 3.2 eV [31], but thin films and
 7 nanoparticles are reported to have higher band gaps due to surface states and quantum size effect
 8 [32,33]. Thus, the measured band gap agrees with Raman and XRD results suggesting the particles are
 9 mostly anatase TiO₂.



1

2 Figure 6 Absorbance spectra from 300 to 900 nm and band-gap (in inset) of the nanoparticles synthesized at 10 MPa, 50 °C

3 Discussion on synthesis of nanoparticle by PLA in pressurized CO₂, their composition and
 4 phase analysis:

5 During PLA, the laser irradiates the target, ionized target species are ejected and trapped inside laser
 6 induced high temperature plasma plume which occurs over a timescale of hundreds of nanoseconds
 7 followed by formation of clusters and their growth inside the plasma [34–36]. Kato et al. reported
 8 formation of plasma and breakdown of CO₂ in PLA in scCO₂ over a short timescale of few hundred
 9 nanoseconds after the laser pulse hit the target and observed generation of cavitation bubble at 5 μs
 10 and its collapse at around 100 μs [37]. The plasma temperature depending on the CO₂ pressure has
 11 been reported to be 3873–4873 °C by Maehara et al. [38] and 8273–12273 °C by Furusato et al. [39].
 12 The high temperature of plasma decomposes CO₂ into atomic oxygen [37,39], carbon ions and radicals
 13 [37] and carbon monoxide positive ions CO⁺ [39]. Kato et al. reported presence of atomic oxygen and
 14 atomic carbon in addition to atomic target metal species in the optical emission spectra of PLA plasmas
 15 in scCO₂ [37]. The presence of plasma plume formation is followed by formation of a cavitation bubble
 16 wherein species originating from the target and the solvent combine to form the clusters and
 17 nanoparticles, which are released to the ambient solvent upon the collapse of the cavitation bubble.
 18 Lam et al. reported that the cavitation bubble consists mostly of solvent species rather than the

1 ablated material for PLA in liquids at normal pressure [40]. The cavitation bubble in scCO₂ has been
2 reported to expand like in liquid but collapse like in gas with the bubble boundary being ragged having
3 higher surface area compared to PLA in liquid CO₂ [37]. Then the reaction for nanoparticle formation
4 inside the cavitation bubble begins between the ablated target species i.e. Ti ions and solvent species
5 from previously plasma decomposed CO₂ molecules to form titanium oxides. Upon the collapse of the
6 cavitation bubble, the hot nanoparticles are released into the surrounding pressurized CO₂. DFT
7 simulations show that oxygen vacancies in Anatase TiO₂ can act as efficient catalyst to dissociate CO₂
8 and the oxygen from CO₂ heals the vacancy [41]. Simulations show that this occurs at relatively low
9 temperatures (400 K). This mechanism likely plays a role in the formation and further oxidation of
10 titanium oxide nanoparticles. The produced CO has tendency to stay adsorbed and may further
11 dissociate to carbon according to Boudouard reaction ($2\text{CO} = \text{C} + \text{CO}_2$) and initiate the formation of
12 the carbon shell.

13 In cases where the nanoparticles are individual particles, the carbon forms as a shell on top of the
14 particles (such as in Figure 3a, b), whereas for the coalesced clusters of nanoparticles the carbon
15 coating is formed over the whole cluster rather (such as in figure 3d, e) than on the individual particles.
16 Salminen et al. suggested laser-induced heating of the nanoparticles to be crucial for shell formation
17 [42]. Marzum et al. attributed formation of graphitic carbon shell to be catalysed by copper in their
18 study on synthesis of copper-carbon core-shell nanoparticles [30].

19 While rutile-TiO₂ is a more thermodynamically stable phase than anatase-TiO₂ [43], and is a dominant
20 phase in PLA in water [44], in this study, as a result of PLA in pressurized CO₂ (in gaseous, liquid and
21 supercritical states), anatase-TiO₂ was the predominant phase as observed in the Raman and XRD
22 spectra (figure 9, 13). Metastable anatase-TiO₂ once formed does not transform to rutile because of
23 strong binding energy of Ti-O ionic covalent bond, unless melting-like processes are involved [45].

24 Titanium dioxide phases are observed in Raman, XPS and XRD, however, presence of other meta-
25 stable phases, such as Ti₃O₅ and Ti₍₁₎O_(0.5)C_(0.5), was also indicated by the XRD spectra. CO₂ above 760

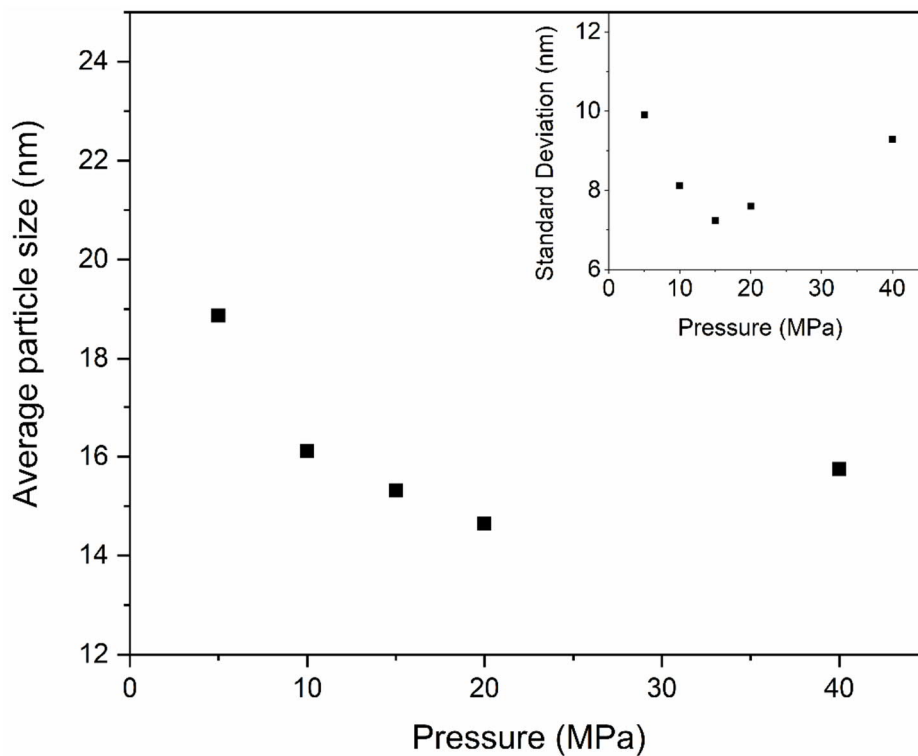
1 °C may undergo Boudouard reaction with carbon to form CO which may reduce TiO₂ to form titanium
2 oxides with lower degree of oxygen such as Ti₃O₅ and further substitution of oxygen with carbon to
3 form Ti_xC_yO_z [46]. Another possibility is that if the temperatures is above 2273 °C, in an environment
4 of excess carbon, TiO₂ and its other oxides are not stable and reduce to Ti(C_xO_y) or TiC, however, a
5 direct conversion from TiO₂ to to Ti(C_xO_y) is not possible without the synthesis of Ti₃O₅ and Ti₂O₃ in
6 between the pathway of this transformation [47]. Observation of Ti₃O₅ and Ti₍₁₎O_(0.5)C_(0.5) in the XRD
7 spectra (figure 9) could either be an indication of oxidation of titanium in insufficient oxygen
8 environment or carbothermal reduction of TiO₂ [47]. The absence of high amounts of rutile-TiO₂ and
9 no observation of TiC may indicate that such high temperatures may not be reached by the
10 synthesized particles to cause phase transformations, however, to some extent transformation may
11 be possible when the nanoparticle size is small enough. Additionally, rutile may form directly without
12 the need of transformation from anatase. The absence of TiC phase could be explained based on
13 thermodynamic calculations. TiO₂ formation from titanium is thermodynamically more favourable
14 than TiC, based on Ellingham diagram. Solving Gibbs free energy equations for TiO₂ and TiC,
15 calculations show TiO₂ formation stays highly favourable until 4529 K.

16 With PLA in pressurized CO₂, we synthesized nanoparticles of metastable anatase-TiO₂ core with
17 carbon layer. However, it is not yet fully understood whether carbon shells on nanoparticles already
18 appear inside the cavitation bubble and whether the particles undergo several coatings of carbon if
19 the ablation durations are long. In-situ studies with small-angle x-ray scattering (SAXS), wide-angle X-
20 ray scattering (WAXS), infrared (IR) and Raman spectroscopy will make good future scope of work to
21 provide insight on this topic.

1 Section 2: Effect of CO₂ pressure and temperature on particle size and phase

2 Effect of CO₂ pressure on nanoparticles

3 The average particle size when plotted for nanoparticles synthesized at 5–40 MPa CO₂ pressures at 50
4 °C temperature showed a decreasing trend from 19 nm to 14.5–15 nm with increasing pressures
5 (figure 7). This is in agreement with the reduction in size of Sn [48], ZnO [49], and Au [26] nanoparticles
6 with an increase in ambient fluid pressure (CO₂, H₂O) as reported in literature by PLA in pressurized
7 fluids. This was attributed to smaller volume and shorter lifetimes of the cavitation bubbles at higher
8 solvent (CO₂, H₂O) pressures [49,50].

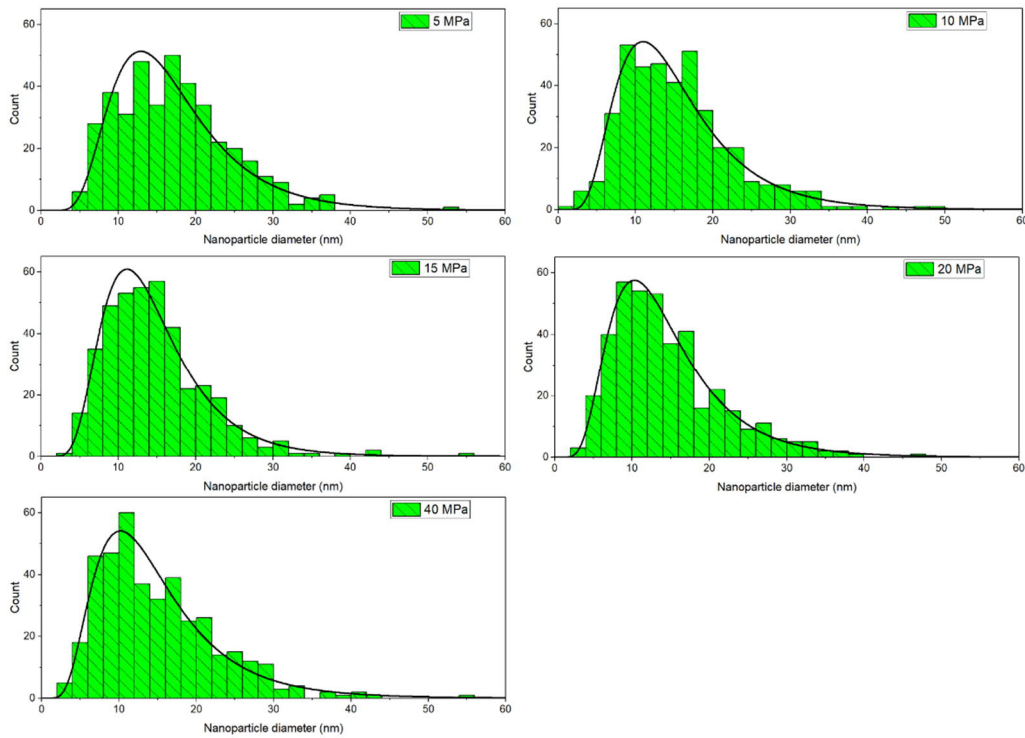


9

10 Figure 7 Variation in nanoparticle size with increase in CO₂ pressure. The inset shows the variation in standard deviation
11 with CO₂ pressure.

12 The size distribution of the synthesized nanoparticles (figure 8) slightly decreased with the increase in
13 pressure. This is observable from the lognormal fitted curves for each size distribution and decreasing

1 trend in the variation of the standard deviation (figure 7 inset). This is in agreement with the narrowing
2 of size distribution with increasing pressures reported for ablation of gold in pressurized CO₂ [26].



3

4

Figure 8 Size distribution of nanoparticles produced from 5-40 MPa at 50 °C.

5 Regarding effect of CO₂ pressure variation on nanoparticle phase, the Raman spectra (figure 9(a))
6 indicated that anatase-TiO₂ is the main phase of the nanoparticles for all samples. Based on the area
7 of the fitted peaks, the rutile content seems to increase with the CO₂ pressure (figure 10(a)). Similarly,
8 the XRD measurements (figure 9(b)) show that the samples are mostly anatase. The area of the fitted
9 peaks in XRD (figure 10(b)) corroborated Raman results and showed an increasing trend. The peak at
10 21.2 2θ degrees corresponding to the high-temperature metastable phase Ti₃O₅ was observed only
11 for 15 MPa CO₂ pressure. XRD and Raman indicated synthesis of mostly anatase-TiO₂ nanoparticles
12 within the range of pressures tested as well as a slight increase in rutile-TiO₂ content as pressure
13 increased.

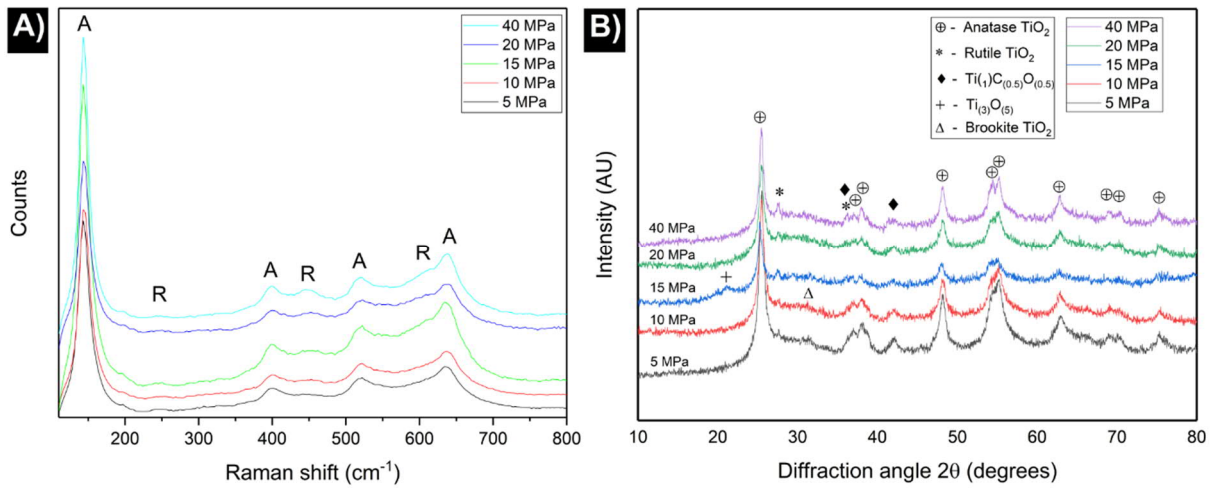


Figure 9 (a) Raman and (b) XRD spectra for nanoparticles synthesized at 50 °C and pressures 5, 10, 15, 20, and 40 MPa.

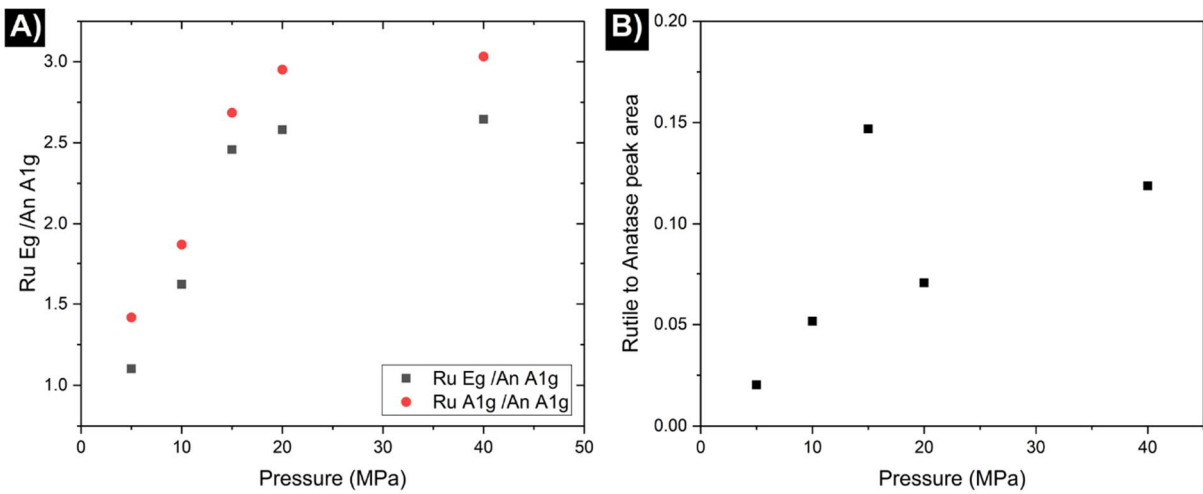
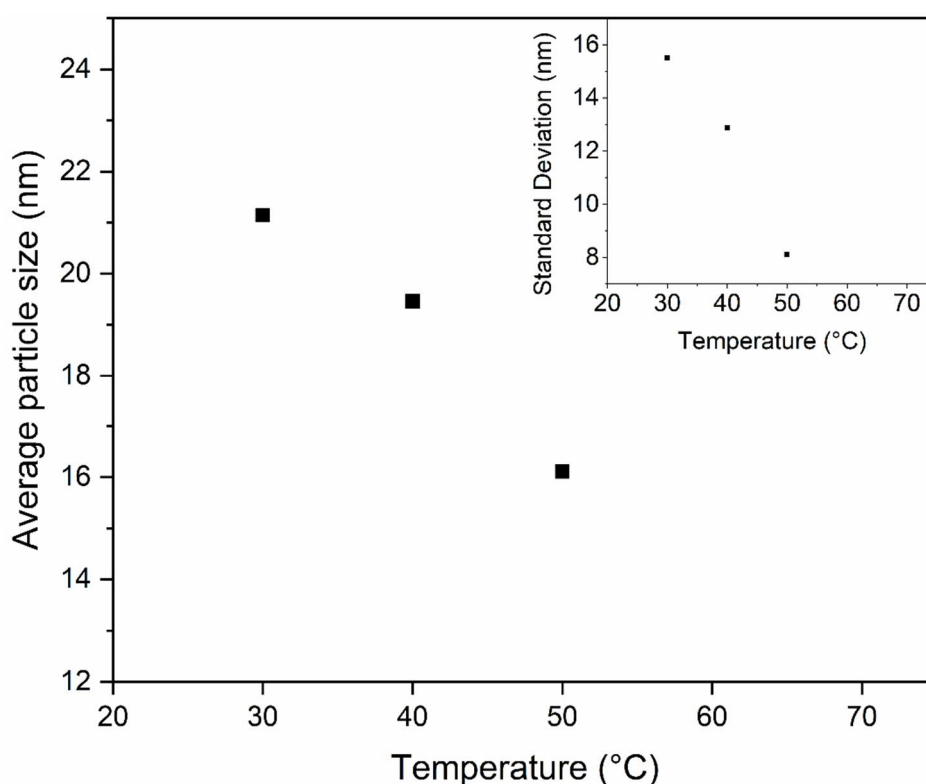


Figure 10 Area of fitted peaks rutile-to-anatase for all pressures from (a) Raman spectra, (b) XRD spectra

Effect of CO₂ temperature on nanoparticles

The influence of CO₂ pressure on cavitation bubble dynamics has been reported in literature [50,51], however, however, the effect of CO₂ temperature has not been studied as much. A clear trend of decreasing nanoparticle size and narrower size distribution was observed with the increase in CO₂ temperature from 30 to 50 °C (figure 11 and figure 12). Although the experimental parameters at 30 °C correspond to liquid CO₂, it is highly likely that the heating due to the laser pulse leads to local conditions corresponding to supercritical CO₂. The trend in the nanoparticle size is somewhat surprising considering that increasing the temperature while keeping the pressure constant leads to a

1 drop in CO₂ density (figure 2), whereas when keeping the temperature constant, the simultaneously
2 increasing pressure and density leads to production of smaller nanoparticles. Cavitation bubble
3 dynamics and its influence on the formed particles has been thoroughly studied in liquids using SAXS
4 [52,53]. To really understand the complex dynamics, a similar comprehensive study for supercritical
5 fluids would be very interesting. Increasing CO₂ temperature showed a slight narrowing of the
6 nanoparticle size distribution (figure 12) corresponding to the decreasing standard deviation (figure
7 11 inset). In this case, the widest size distribution was observed for CO₂ in liquid state i.e. at 30 °C.



8

9 Figure 11 Effect of CO₂ Temperature on nanoparticle size; in the inset is reported the variation of standard deviation with
10 CO₂ temperature.

11

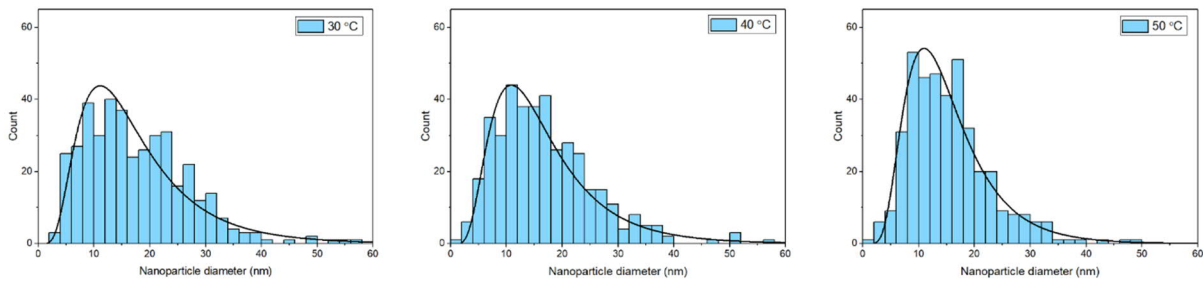


Figure 12 Size distribution of nanoparticles synthesized at 10 MPa and temperatures 30, 40, and 50 °C.

XRD and Raman indicated the main phase of nanoparticles was anatase-TiO₂ and remained unchanged despite the change in CO₂ temperature from 30–50 °C (figure 13(a, b)). Unlike in CO₂ pressure variation, in case of CO₂ temperature variation, a conclusive trend on variation in rutile amount could not be observed.

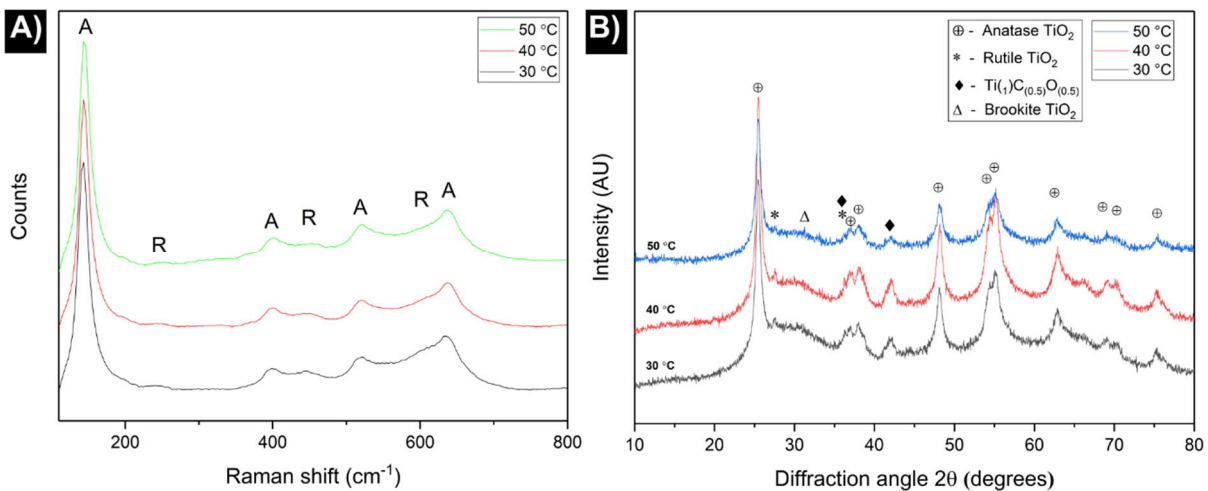


Figure 13 (a) Raman and (b) XRD spectra for nanoparticles synthesized at 10 MPa and temperatures 30, 40, and 50 °C.

Amongst the tested process conditions, the lowest temperature and the lowest pressure test conditions i.e. 30 °C, 10 MPa (gaseous CO₂) and 50 °C, 5 MPa (liquid CO₂) respectively, are interesting as they are both not supercritical conditions for CO₂. When compared these two extreme test conditions to all other test conditions, the nanoparticle sizes were the highest and size distributions among the widest in non-supercritical conditions. This may imply that PLA in CO₂ in supercritical conditions produced nanoparticles with smaller size and slightly narrower size distribution than in

1 liquid (at same temperature) or gaseous state (at same pressure). In addition, regarding the minor
2 phase, the rutile content was among the least for the tests in non-supercritical conditions.

3 Conclusions

4 To the best of our knowledge, this is the first study that demonstrates PLA in liquid, gaseous and
5 supercritical CO₂ for production of TiO₂-carbon core-shell nanoparticles. STEM-EDS showed the
6 nanoparticles were mostly round with either carbon layers on them individually like a shell or
7 coalesced nanoparticles collectively covered with carbon layers. STEM backscatter topography mode
8 elucidated this observation. XPS, Raman and XRD indicated anatase-TiO₂ as the main phase of
9 nanoparticles with minor amounts of rutile-TiO₂, and possibility of presence of brookite-TiO₂,
10 Ti₍₁₎O_(0.5)C_(0.5), and Ti₃O₅. Although, Ti₍₁₎O_(0.5)C_(0.5) phase was detected in XRD, XPS indicated that carbon
11 was not bonded to titanium. This was further corroborated by XRD and Raman results. The bandgap
12 energy of these nanoparticles was calculated to be 3.32 eV.

13 Increase in CO₂ pressure from 5 to 40 MPa at 50 °C led to decrease in the nanoparticle size and
14 narrowing of the size distribution. The mechanism of size refinement was attributed to shorter
15 cavitation bubble lifetime and smaller volume at higher pressures. From Raman and XRD spectra, we
16 observed that anatase-TiO₂ was the main phase of nanoparticles in all CO₂ pressures 5–40 MPa tested
17 at 50 °C. The ratio of area of the fitted rutile-anatase peaks indicated increase in rutile content with
18 increase in pressure in both Raman and XRD. Further, when the CO₂ temperature was varied from 30–
19 50 °C at 10 MPa pressure, we observed decreasing trend in particle size and narrowing of size
20 distribution. In this case, we observed anatase-TiO₂ as the main phase of nanoparticles at all
21 temperatures, however, the variation in the amount of rutile-TiO₂ could not be conclusively
22 determined based on peaks in Raman and XRD spectra.

23 For future work, in-situ studies with SAXS, WAXS, IR and Raman microscopy would be crucial to give
24 insight on the process dynamics, nanoparticle nucleation, and breakdown of CO₂ with variation in CO₂

1 parameters. For this, the autoclave will have to be modified to accommodate the measurement
2 systems.

3 Acknowledgements

4 This work was supported by European Commission's Horizon 2020 project 'NanoStencil' - Proposal
5 number 767285. This work made use of Tampere Microscopy Center facilities at Tampere University.

6 We would like to acknowledge Jere Manni for XPS studies performed at Top Analytica.

7 Declaration

8 The authors declare no conflict of interest.

9 References

- 10 [1] Friedmann D, Mendive C and Bahnemann D 2010 TiO₂ for water treatment: Parameters
11 affecting the kinetics and mechanisms of photocatalysis Appl. Catal. B Environ. 99 398–406
- 12 [2] Exnar I, Kavan L, Huang S Y and Grätzel M 1997 Novel 2 V rocking-chair lithium battery based
13 on nano-crystalline titanium dioxide J. Power Sources 68 720–2
- 14 [3] Tennakone K, Kumarasinghe A R, Sirimanne P M and Kumara G R R A 1995 Deposition of thin
15 polycrystalline films of cuprous thiocyanate on conducting glass and photoelectrochemical
16 dye-sensitization Thin Solid Films 261 307–10
- 17 [4] Park J, Back T, Mitchel W C, Kim S S, Elhamri S, Boeckl J, Fairchild S B, Naik R and Voevodin A A
18 2015 Approach to multifunctional device platform with epitaxial graphene on transition metal
19 oxide Sci. Rep. 5 14374
- 20 [5] Lee J-M, Han S-B, Kim J-Y, Lee Y-W, Ko A-R, Roh B, Hwang I and Park K-W 2010 TiO₂@carbon
21 core-shell nanostructure supports for platinum and their use for methanol electrooxidation
22 Carbon N. Y. 48 2290–6
- 23 [6] Gawande M B, Goswami A, Asefa T, Guo H, Biradar A V, Peng D, Zboril R and Varma R S 2015

- 1 Core-shell nanoparticles: synthesis and applications in catalysis and electrocatalysis Chem. Soc.
2 Rev. 44 7540–90
- 3 [7] Feng H, Tang L, Zeng G, Zhou Y, Deng Y, Ren X, Song B, Liang C, Wei M and Yu J 2019 Core-shell
4 nanomaterials: Applications in energy storage and conversion Adv. Colloid Interface Sci. 267
5 26–46
- 6 [8] Kumar K S, Kumar V B and Paik P 2013 Recent Advancement in Functional Core-Shell
7 Nanoparticles of Polymers: Synthesis, Physical Properties, and Applications in Medical
8 Biotechnology J. Nanoparticles 2013 1–24
- 9 [9] Chang W, Skandan G, Hahn H, Danforth S C and Kear B H 1994 Chemical vapor condensation
10 of nanostructured ceramic powders Nanostructured Mater. 4 345–51
- 11 [10] Kobayashi Y, Correa-Duarte M A and Liz-Marzán L M 2001 Sol-Gel Processing of Silica-Coated
12 Gold Nanoparticles Langmuir 17 6375–9
- 13 [11] Wang Y, Teng X, Wang J-S and Yang H 2003 Solvent-Free Atom Transfer Radical Polymerization
14 in the Synthesis of Fe₂O₃ @Polystyrene Core-Shell Nanoparticles Nano Lett. 3 789–93
- 15 [12] Biswas P, Wu C Y, Zachariah M R and McMillin B 1997 Characterization of iron oxide-silica
16 nanocomposites in flames: Part II. Comparison of discrete-sectional model predictions to
17 experimental data J. Mater. Res. 12 714–23
- 18 [13] Chen K Z, Zhang Z K, Cui Z L, Zuo D H and Yang D Z 1997 Catalytic properties of nanostructured
19 hydrogen storage nickel particles with cerium shell structure Nanostructured Mater. 8 205–13
- 20 [14] Vollath D and Szabo D V 1999 Coated Nanoparticles: A New Way to Improved Nanocomposites
21 J. Nanoparticle Res. 1 235–42
- 22 [15] Yu F, Wang J N, Sheng Z M and Su L F 2005 Synthesis of carbon-encapsulated magnetic
23 nanoparticles by spray pyrolysis of iron carbonyl and ethanol Carbon N. Y. 43 3018–21

- 1 [16] Kazakevich P V, Simakin A V, Voronov V V, Shafeev G A, Starikov D and Bensaoula A 2005
2 Formation of Core-Shell Nanoparticles by Laser Ablation of Copper and Brass in Liquids Solid
3 State Phenom. 106 23–6
- 4 [17] Zhang D, Gökce B and Barcikowski S 2017 Laser Synthesis and Processing of Colloids:
5 Fundamentals and Applications Chem. Rev. 117 3990–4103
- 6 [18] Singh A, Salminen T, Honkanen M, Vihinen J, Hyvärinen L and Levänen E 2019 Multiphase Ti_xO_y
7 nanoparticles by pulsed laser ablation of titanium in supercritical CO_2 Appl. Surf. Sci. 476 822-
8 7
- 9 [19] Saitow K, Yamamura T and Minami T 2008 Gold nanospheres and nanonecklaces generated by
10 laser ablation in supercritical fluid J. Phys. Chem. C 112 18340–9
- 11 [20] Saitow K 2005 Silicon Nanoclusters Selectively Generated by Laser Ablation in Supercritical
12 Fluid J. Phys. Chem. B 109 3731–3
- 13 [21] Machmudah S, Sato T, Wahyudiono, Sasaki M and Goto M 2012 Silver nanoparticles generated
14 by pulsed laser ablation in supercritical CO_2 medium High Press. Res. 32 60–6
- 15 [22] Kuwahara Y, Saito T, Haba M, Iwanaga T, Sasaki M and Goto M 2009 Nanosecond Pulsed Laser
16 Ablation of Copper in Supercritical Carbon Dioxide Jpn. J. Appl. Phys. 48 040207
- 17 [23] Nakahara S, Stauss S, Kato T, Sasaki T and Terashima K 2011 Synthesis of higher diamondoids
18 by pulsed laser ablation plasmas in supercritical CO_2 J. Appl. Phys. 109 123304 (1-8)
- 19 [24] Machmudah S, Kuwahara Y, Sasaki M and Goto M 2011 Nano-structured particles production
20 using pulsed laser ablation of gold plate in supercritical CO_2 J. Supercrit. Fluids 60 63–8
- 21 [25] Mardis M, Takada N, Machmudah S, Wahyudiono, Sasaki K, Kanda H and Goto M 2016 Nickel
22 nanoparticles generated by pulsed laser ablation in liquid CO_2 Res. Chem. Intermed. 42 4581–
23 90

- 1 [26] Mardis M, Wahyudiono, Takada N, Kanda H and Goto M 2018 Formation of Au-carbon
2 nanoparticles by laser ablation under pressurized CO₂ Asia-Pacific J. Chem. Eng. 13 e2176
- 3 [27] National Institute of Standards and Technology US Department of Commerce Thermophysical
4 Properties for Carbon dioxide - NIST Chemistry WebBook, SRD 69 Natl. Inst. Stand. Technol.
- 5 [28] Jung H J and Choi M Y 2018 One-pot synthesis of graphitic and nitrogen-doped graphitic layers
6 on nickel nanoparticles produced by pulsed laser ablation in liquid: Solvent as the carbon and
7 nitrogen source Appl. Surf. Sci. 457 1050–6
- 8 [29] Wagener P, Jakobi J, Rehbock C, Chakravadhanula V S K, Thede C, Wiedwald U, Bartsch M,
9 Kienle L and Barcikowski S 2016 Solvent-surface interactions control the phase structure in
10 laser-generated iron-gold core-shell nanoparticles Sci. Rep. 6 1–12
- 11 [30] Marzun G, Bönnemann H, Lehmann C, Spliethoff B, Weidenthaler C and Barcikowski S 2017
12 Role of Dissolved and Molecular Oxygen on Cu and PtCu Alloy Particle Structure during Laser
13 Ablation Synthesis in Liquids ChemPhysChem 18 1175–84
- 14 [31] Reyes-Coronado D, Rodríguez-Gattorno G, Espinosa-Pesqueira M E, Cab C, de Coss R and
15 Oskam G 2008 Phase-pure TiO₂ nanoparticles: anatase, brookite and rutile Nanotechnology
16 19 145605
- 17 [32] Wang Y and Herron N 1991 Nanometer-sized semiconductor clusters: materials synthesis,
18 quantum size effects, and photophysical properties J. Phys. Chem. 95 525–32
- 19 [33] Madhusudan Reddy K, Manorama S V and Ramachandra Reddy A 2003 Bandgap studies on
20 anatase titanium dioxide nanoparticles Mater. Chem. Phys. 78 239–45
- 21 [34] Amendola V and Meneghetti M 2013 What controls the composition and the structure of
22 nanomaterials generated by laser ablation in liquid solution? Phys. Chem. Chem. Phys. 15
23 3027–46

- 1 [35] Shih C-Y, Wu C, Shugaev M V. and Zhigilei L V. 2017 Atomistic modeling of nanoparticle
2 generation in short pulse laser ablation of thin metal films in water J. Colloid Interface Sci. 489
3 3–17
- 4 [36] Amendola V and Meneghetti M 2009 Laser ablation synthesis in solution and size manipulation
5 of noble metal nanoparticles. Phys. Chem. Chem. Phys. 11 3805–21
- 6 [37] Kato T, Stauss S, Kato S, Urabe K, Baba M, Suemoto T and Terashima K 2012 Pulsed laser
7 ablation plasmas generated in CO₂ under high-pressure conditions up to supercritical fluid
8 Appl. Phys. Lett. 101 224103
- 9 [38] Maehara T, Kawashima A, Iwamae A, Mukasa S, Takemori T, Watanabe T, Kurokawa K, Toyota
10 H and Nomura S 2009 Spectroscopic measurements of high frequency plasma in supercritical
11 carbon dioxide Phys. Plasmas 16 033503
- 12 [39] Furusato T, Ashizuka N, Kamagahara T, Matsuda Y, Yamashita T, Sasaki M, Kiyon T and Inada Y
13 2018 Anomalous plasma temperature at supercritical phase of pressurized CO₂
14 after pulsed breakdown followed by large short-circuit current IEEE Trans. Dielectr. Electr. Insul.
15 25 1807–13
- 16 [40] Lam J, Lombard J, Dujardin C, Ledoux G, Merabia S and Amans D 2016 Dynamical study of
17 bubble expansion following laser ablation in liquids Appl. Phys. Lett. 108 074104
- 18 [41] Huygh S, Bogaerts A and Neyts E C 2016 How Oxygen Vacancies Activate CO₂ Dissociation on
19 TiO₂ Anatase (001) J. Phys. Chem. C 120 21659–69
- 20 [42] Salminen T, Honkanen M and Niemi T 2013 Coating of gold nanoparticles made by pulsed laser
21 ablation in liquids with silica shells by simultaneous chemical synthesis Phys. Chem. Chem.
22 Phys. 15 3047–51
- 23 [43] Cui Z-H, Wu F and Jiang H 2016 First-principles study of relative stability of rutile and anatase
24 TiO₂ using the random phase approximation Phys. Chem. Chem. Phys. 18 29914–22

- 1 [44] Singh A, Vihinen J, Frankberg E, Hyvärinen L, Honkanen M and Levänen E 2016 Pulsed Laser
2 Ablation-Induced Green Synthesis of TiO₂ Nanoparticles and Application of Novel Small Angle
3 X-Ray Scattering Technique for Nanoparticle Size and Size Distribution Analysis *Nanoscale Res.*
4 *Lett.* 11 447
- 5 [45] Satoh N, Nakashima T and Yamamoto K 2013 Metastability of anatase: size dependent and
6 irreversible anatase-rutile phase transition in atomic-level precise titania *Sci. Rep.* 3 1959
- 7 [46] Hajalilou A, Hashim M, Ebrahimi-Kahizsangi R, Ismail I and Sarami N 2014 Synthesis of titanium
8 carbide and TiC–SiO₂ nanocomposite powder using rutile and Si by mechanically activated
9 sintering *Adv. Powder Technol.* 25 1094–102
- 10 [47] Kim J and Kang S 2014 Stable phase domains of the TiO₂–Ti₃O₅–Ti₂O₃–TiO–Ti(C_xO_y)–TiC system
11 examined experimentally and via first principles calculations *J. Mater. Chem. A* 2 2641–7
- 12 [48] Koizumi M, Kulinich S A, Shimizu Y and Ito T 2013 Slow dynamics of ablated zone observed
13 around the density fluctuation ridge of fluid medium *J. Appl. Phys.* 114 214301
- 14 [49] Kulinich S A, Kondo T, Shimizu Y and Ito T 2013 Pressure effect on ZnO nanoparticles prepared
15 via laser ablation in water *J. Appl. Phys.* 113 033509
- 16 [50] Sasaki K, Nakano T, Soliman W and Takada N 2009 Effect of Pressurization on the Dynamics of
17 a Cavitation Bubble Induced by Liquid-Phase Laser Ablation *Appl. Phys. Express* 2 046501
- 18 [51] Takada N and Machmudah S 2014 Characteristics of optical emission intensities and bubblelike
19 phenomena induced by laser ablation in supercritical fluids *Jpn. J. Appl. Phys.* 010213
- 20 [52] Wagener P, Ibrahimkuty S, Menzel A, Plech A and Barcikowski S 2013 Dynamics of silver
21 nanoparticle formation and agglomeration inside the cavitation bubble after pulsed laser
22 ablation in liquid *Phys. Chem. Chem. Phys.* 15 3068–74

1 [53] Ibrahimkuty S, Wagener P, Rolo T D S, Karpov D, Menzel A, Baumbach T, Barcikowski S and
2 Plech A 2015 A hierarchical view on material formation during pulsed-laser synthesis of
3 nanoparticles in liquid Sci. Rep. 5 16313

4